PERGAMON

International Journal of Heat and Mass Transfer 42 (1999) 1371–1382

International Journal of HEAT and MASS TRANSFER

Experimental and numerical investigation of heat transfer and phase change phenomena during excimer laser interaction with nickel

X. Xu*, G. Chen, K.H. Song

School of Mechanical Engineering, Purdue University, West Lafayette, IN 47907, U.S.A.

Received 18 June 1998; in final form 6 August 1998

Abstract

This work investigates heat transfer and phase change phenomena during excimer laser interaction with nickel specimens. Based on time-resolved measurements in the laser fluence range between 2.5 J cm^{-2} and 10.5 J cm^{-2}, it is found that surface evaporation occurs when the laser fluence is below 5.2 J cm^{-2}. At a laser fluence of 5.2 J cm^{-2} or higher, explosive-type vaporization takes place. Numerical calculations show the maximum surface temperature reaches $0.84T_c$ at a laser fluence of 5.2 J cm^{-2}, and $0.9T_c$ at a laser fluence of 5.9 J cm^{-2}. The numerical results agree with the experiments on the mechanisms of materials removal in different laser fluence regions.

Key words: Pulsed laser; Homogeneous nucleation; Explosive phase transformation; Heat transfer

Nomenclature

A coefficient in equation (9)
c_p specific heat [J (kg^{-1} K^{-1})]
C_0, C_1 constants in equations (3) and (4)
d thickness of the specimen [m]
f volume fraction
i imaginary unit
I laser intensity [W m^{-2}]
j_v molar evaporation flux [mol (m^{-2} s^{-1})]
k_b Boltzmann's constant, 1.380×10^{-23} J K^{-1}
k thermal conductivity [W (m^{-1} K^{-1})]
L_{lv} latent heat of evaporation [J kg^{-1}]
L_{sl} latent heat of fusion [J kg^{-1}]
M molar weight [kg kmol^{-1}]
$\hat{n}$ complex index of refraction
n, k real and imaginary part of the complex index of refraction
p pressure [N m^{-2}]
Q constant in equation (3)
Q_a volumetric absorption [W m^{-3}]
R universal gas constant, 8.314 kJ kmol^{-1} K^{-1}
R_f reflectivity
t time [s]
T_c critical temperature [K]
T_m equilibrium melting temperature [K]
V velocity [m s^{-1}]
x coordinate perpendicular to the target surface [m].

Greek symbols

α absorption coefficient [m^{-1}]
δ diameter of the hole in the specimen (Fig. 2(b)) [m]
ΔT interface superheating [K]
θ angle of incidence
λ_{exc} excimer laser wavelength [m]
ρ density [kg m^{-3}]
τ transmissivity.

Subscripts

l liquid
lv liquid–vapor interface
Ni nickel
s solid
sl solid–liquid interface
0 room temperature.

* Corresponding author. Tel.: 001 765 494 5639; fax: 001 765 494 9539; e-mail: xxu@ecn.purdue.edu

0017–9310/98/$ - see front matter
PII: S0017–9310(98)00272–5

1. Introduction

High power, nanosecond pulsed excimer lasers are finding many attractive applications. Examples include thin film deposition and micro-machining. In these applications, the energy of the laser beam is utilized to induce rapid evaporation of the target materials. Understanding the mechanisms of the laser evaporation process would be helpful to the applications involving the use of excimer lasers.

High power laser induced evaporation has been studied extensively. Miotello and Kelly [1] suggested explosive vaporization could occur at high laser fluences. According to Miotello and Kelly, when the laser fluence is sufficiently high and the pulse length is sufficiently short, the temperature of the specimen could be raised to well above its boiling temperature. At a temperature of about $0.9T_c$ (T_c is the thermodynamic critical temperature) homogeneous bubble nucleation occurs. The surface undergoes a rapid transition from superheated liquid to a mixture of vapor and liquid droplets.

The explosive phase change phenomenon was first investigated in detail in the earlier work of pulsed current heating of metals [2, 3]. Figure 1(a) shows the phase diagram from the boiling point to the critical temperature. When the heating rate is low, the liquid and vapor above the liquid surface are in equilibrium, and their states are represented by the binode line that is calculated from the Clausius–Clapeyron equation. Under rapid heating, it is possible to superheat the liquid metal to a metastable state, i.e., the surface pressure is lower than the saturation pressure corresponding to the surface temperature. The relation between the surface pressure and the saturation pressure can be obtained considering the conservation requirements across the discontinuity layer above the liquid surface [4, 5]. Intense fluctuation starts to occur in the metastable liquid when its temperature approaches $0.8T_c$, which drastically affects physical properties, including density, specific heat, electric resistance, and optical constants as shown in Fig. 1(b). When the temperature reaches about $0.9T_c$, the spinode, the rate of spontaneous bubble nucleation in the melt increases drastically. The rate of spontaneous nucleation can be computed using the Döring and Volmer's theory [6]. It has been shown that the spontaneous nucleation rate is about 1 s^{-1} cm^{-3} at the temperature of $0.87T_c$, but increases to 10^{26} s^{-1} cm^{-3} at $0.91T_c$ [3]. This large change in nucleation rate indicates a rapidly heated liquid could possess considerable stability with respect to spontaneous nucleation, with an avalanche-like onset of spontaneous nucleation of the entire high temperature liquid layer at about $0.9T_c$. The exact spinodal temperature can be calculated from the second derivatives of the Gibbs' thermodynamic potential when the equation of state near the critical point is available [2].

During pulsed excimer laser heating, radiation energy from the laser beam is transformed to thermal energy within the radiation penetration depth, which is about 10 nm for Ni at the KrF excimer laser wavelength. Superheating is possible since the excimer laser pulse is short, on the order of 10^{-8} s. Within this time duration, the amount of nuclei generated by spontaneous nucleation is small at temperatures below $0.9T_c$, thus the liquid can be heated to the metastable state. Heterogeneous evaporation always occurs at the liquid surface, however, when the laser intensity is high enough to induce explosive phase transformation, physical phenomena associated with laser ablation are dominated by explosive vaporization.

In this paper, we present experimental data of pulsed excimer laser ablation of nickel specimens. Properties of the laser-evaporated plume, which consists weakly ionized vapor and possibly liquid droplets due to explosive phase transformation, are studied. Time-resolved measurements are performed to determine the velocity and optical properties of the laser-ablated plume in the laser fluence range between 2.5 and 10.5 J cm^{-2}. These experimental studies have shown distinct phenomena when the laser fluence is varied across 5.2 J cm^{-2}, suggesting different phase change mechanisms in different laser fluence regimes. Numerical simulations of pulsed laser ablation are also performed to further validate the evaporation theories. In the computation, heating above the normal melting and boiling temperatures is allowed by including interface kinetic relations. The measured temporal variation of the laser pulse energy and surface reflectivity, and temperature dependent thermophysical properties are used as input parameters. Further, absorption of laser energy by the laser-evaporated plume is accounted for by using the measured transient transmissivity of the excimer laser beam through the laser-evaporated plume. Results of the numerical simulation compare well with the experimentally determined threshold value of the onset of explosive phase transformation. Finally, numerical sensitivity studies are performed to determine the effect of uncertain thermophysical properties and interfacial relations on the computational results.

2. Experimental study

Experimental studies include measurements of velocity and optical properties of the laser-evaporated plume. A KrF excimer laser with a wavelength of 248 nm and a pulse width of 26 ns (FWHM, full width at half maximum) is used. The laser fluence is varied from 2.5 to 10.5 J cm^{-2}. A 99.94% pure nickel specimen is used as the ablation target. Experimental apparatus and procedures are described in detail in previous publications [7, 8]. Only a brief description of each experiment is given here.

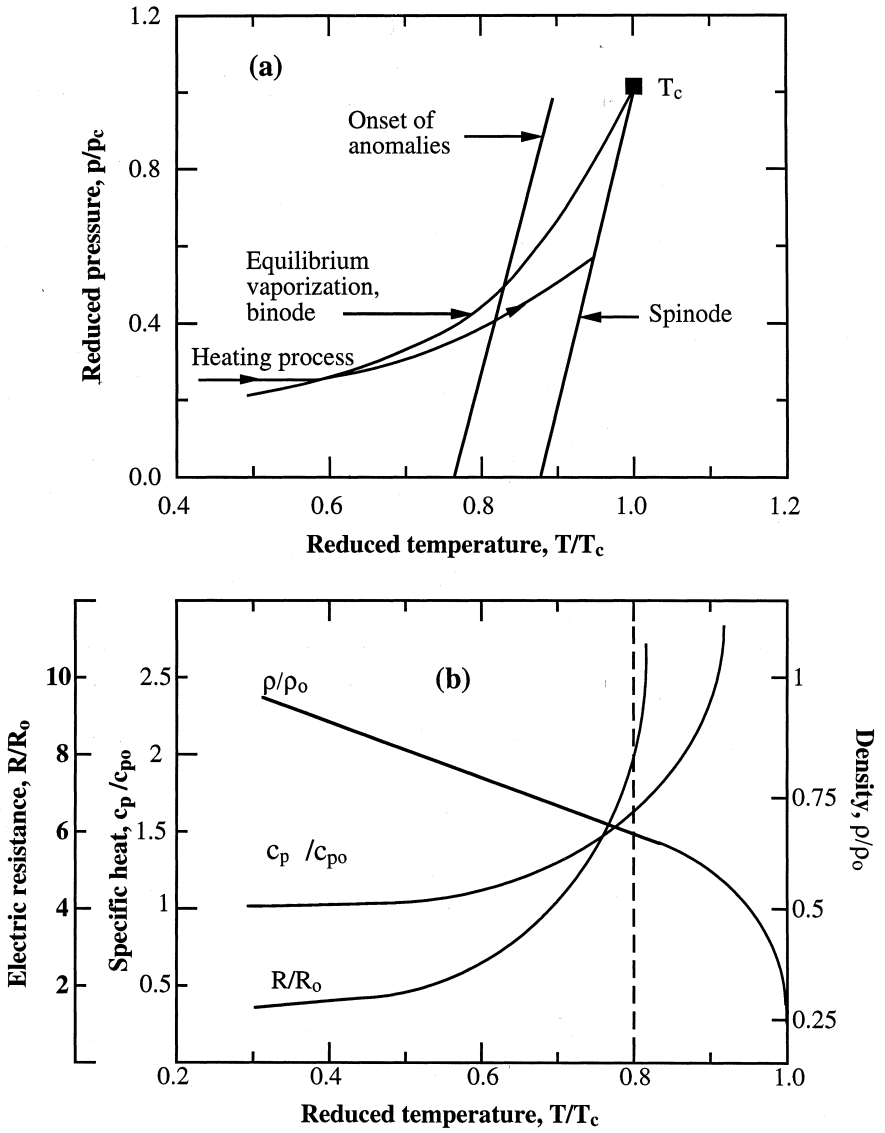

Fig. 1. (a) p–T diagram and (b) typical variations of physical properties of liquid metal near the critical point. The substrate '0' denotes properties at the normal boiling temperature [3].

An optical deflection technique is employed to measure the velocity of the laser-ablated plume. As shown in Fig. 2(a), a probing HeNe laser beam traveling parallel to the target surface passes through the laser-ablated plume. When laser ablation occurs, the intensity of the probing beam is disturbed due to discontinuity of optical properties across the laser-induced shock wave, and due to scattering and absorption by the plume. The distance between the probing beam and the target surface is incrementally adjusted and the corresponding arrival time of the probing beam fluctuation is recorded. The velocity of the laser-ablated plume is obtained from the measured distance–time relation.

Figure 2(b) illustrates the measurement of transmission of the laser-ablated plume at the excimer laser wavelength. A probing beam separated from the excimer laser beam passes through the plume and a small hole (diameter ~ 10 μm) fabricated on the specimen, which is a free-standing nickel foil with a thickness of about 6 μm. The heating laser beam irradiates the target at normal

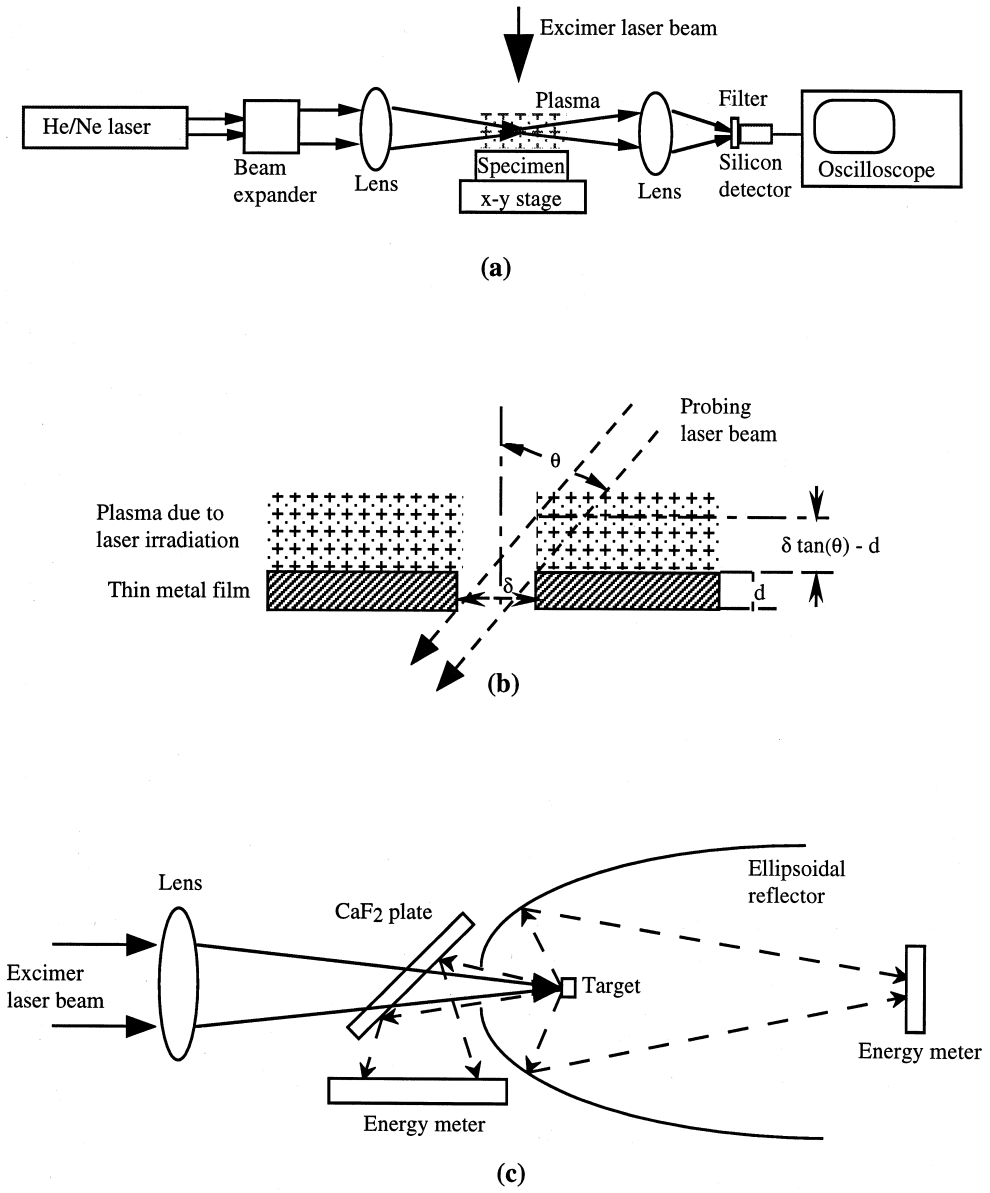

Fig. 2. Experimental set-up for measuring (a) the velocity of the plasma front, (b) transmission of the laser beam through the plasma, and (c) the laser energy lost to the ambient.

direction and the angle of incidence of the probing beam is 45°. This configuration ensures detection of transmission of the probing beam in the plume when the plume thickness is greater than $\varphi \tan(\theta) - d$, which corresponds to 4 μm in this experiment.

Scattering of the laser beam from the plume is measured from the back of the specimen at different angles. The experimental setup is similar to that for the transmission measurement, except that the diameter of the hole in the specimen is about 100 μm. The total laser energy loss to the ambient due to scattering from the plume and reflection from the target surface is measured with the use of an ellipsoidal reflector (Fig. 2(c)). The amount of laser energy not absorbed by the target and the laser generated plume is measured by the two energy meters. The percentages of laser energy absorbed by the plume, lost to the ambient, and absorbed by the target are calculated from the results of the transmissivity, scattering and total energy loss measurements [7].

Results of the measured velocity of the laser-ablated

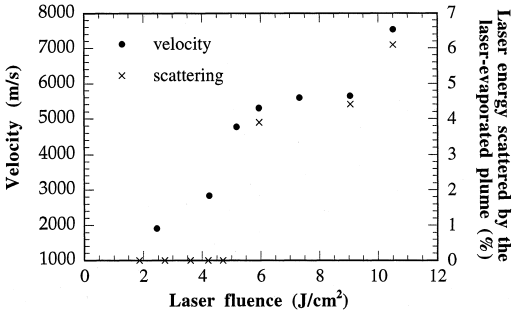

Fig. 3. Velocity of the plume front and laser energy scattered by the laser-evaporated plume as a function of laser fluence.

plume, the percentage of laser energy scattered from the plume and the transmissivity of the plume are summarized in Figs 3 and 4. According to these results, the laser fluence range used in the experiment can be divided into three regions: the low fluence region with laser fluences between 2.5 and 5.2 J cm^{-2}, the medium fluence region with laser fluences between 5.2 and 9.0 J cm^{-2}, and the high fluence region with laser fluences above 9.0 J cm^{-2}.

Figure 3 shows variations of the plume velocity with the laser fluence. The probing beam in the optical deflection measurement is disturbed by both the shock wave and the laser generated plume, therefore, both the shock velocity and the plume front velocity can be determined [8]. The first fluctuation of the optical deflection signal is caused by the shock wave which is a thin layer of discontinuity in the optical refractive index, and the second fluctuation is caused by the laser-induced plasma plume. The time elapse between these two fluctuations is within a few nanoseconds when the distance between the probing beam and the target surface is of the order of a hundred micrometers. However, when the probing beam is located at distances closer to the target surface (less than 100 μm), the two fluctuations are indistinguishable since the distance between the shock front and the vapor front is less than the measurement resolution. Figure 3 shows the velocity values of the plume front averaged within the time period from the onset of evaporation to the end of the laser pulse. Within the laser pulse, the shock front velocity (not shown in the figure) is about 10% higher than the velocity of the plume front. The plume velocity increases with the laser fluence increase, from $\sim$2000 m s^{-1} at the lowest laser fluence to $\sim$8000 m s^{-1} at the highest fluence. However, the increase of velocity is not monotonous; the velocity is almost a constant in the medium fluence region. The velocity of the evaporating plume is determined by the pressure and temperature at the target surface. The constant velocity in the medium fluence region indicates that the peak surface temperature is not affected by the increase of the laser fluence in this fluence region. Such a constant surface temperature can be explained as a result of explosive evaporation. As has been discussed, the maximum surface temperature during explosive phase transformation is about $0.9T_c$, the spinodal temperature. Once the laser fluence is high enough to raise the surface temperature to the spinode, increase of the laser fluence would not raise the surface temperature further. On the other hand, in the low fluence region, the velocity increases over 50%. Therefore, the surface temperature increases with the laser fluence increase; heterogeneous vaporization occurs at the surface. At the highest laser fluence, the velocity of the plume is higher than that of the middle fluence region. This could be due to a higher absorption rate of the laser energy by the plume, as shown in the transmission measurement (Fig. 4). Absorption of laser energy by the plume further raises the temperature of the plume and increases the plume velocity.

Figure 3 also shows the percentage of laser energy

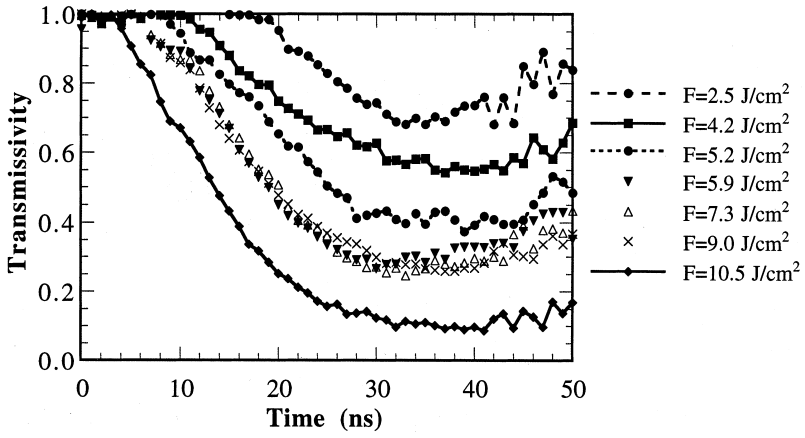

Fig. 4. Transient transmissivity of the laser beam through the laser-ablated plume.

scattered from the plume (part of the energy lost to the ambient) as a function of laser fluence. The size of the particles in the plume that scattered the laser beam was measured to be about 120 nm [7], therefore, scattering is mainly due to large size liquid droplets. It is seen from Fig. 3 that there is almost no scattering (less than 0.5%, the measurement resolution) in the low laser fluence region. Therefore, there is almost no large size liquid droplets in the plume. When the laser fluence is higher than 5.2 J cm^{-2}, the percentage of laser energy scattered by the plume is about 4–6%, indicating the existence of liquid droplets in the plume. This phenomenon again can be explained by explosive phase transformation. When explosive phase change occurs, the entire surface layer with a temperature near $0.9T_c$ is evaporated from the target. The recoil pressure caused by explosive vaporization is high enough to flush out liquid from the molten pool. The evaporant during explosive evaporation is a mixture of atomic vapor (charged or neutral), electrons and liquid droplets. Therefore, the result of the scattering measurement provides a direct indication of the transition from heterogeneous evaporation to explosive phase transformation at the laser fluence around 5.2 J cm^{-2}.

Figure 4 shows the transient transmissivity of a probing beam at the excimer laser wavelength passing through the laser evaporated plume. The transmissivity remains at one for the first several nanoseconds, which is the time duration before evaporation occurs. Transmissivities below one indicate absorption by the laser-generated plume. As expected, evaporation occurs at an earlier time at higher laser fluences so that transmissivity starts to decrease earlier at higher fluences. Transmission decreases with the increase of the laser fluence, however, it does not change with the laser fluence in the medium fluence region, i.e., extinction of the laser beam in the plume does not vary with the laser intensity in the medium fluence region. Extinction of the laser beam is determined by the cross section of energized atoms that is determined by the temperature of the plume, and the number density of the evaporant. Therefore, there is no change in the number density and the temperature of the plume in the medium fluence range. As discussed before, temperatures of the evaporant in the medium fluence range are all about $0.9T_c$ due to explosive phase transformation. Therefore, the transmission data again indicate explosive phase transformation at laser fluences higher than 5.2 J cm^{-2}. At the highest laser fluence, transmissivity decreases from that of the middle fluence range, indicating the increase of absorption by the plume.

In summarizing the experimental results different dynamic and optical behaviors of the laser ablated plume are found in different laser fluence regions. These phenomena can be explained by different evaporation mechanisms at the target surface. The transition from the surface evaporation to homogeneous, explosive phase change occurs at a laser fluence of about 5.2 J cm^{-2}.

3. Numerical modeling

Numerical modeling is carried out to compute the heat transfer and phase change processes during excimer laser evaporation. The following effects are taken into consideration: reflection and absorption of the laser beam at the material surface; heat conduction in the material, melting and evaporation. Due to the high temperature of the evaporated vapor, the interaction between the vapor/plasma plume and the laser beam is also considered.

3.1. Governing equations

A one-dimensional heat conduction model is used to calculate heating and phase transformation in the target. The one-dimensional model is appropriate since excimer laser energy is distributed evenly over the target surface in a rectangular domain, instead of a Gaussian distribution commonly seen for other types of laser. The size of the laser spot on the target surface is several millimeters, while the heat diffusion depth is of the order of several micrometers, therefore, heat transfer at the center of the laser beam is essentially one-dimensional. The one-dimensional heat conduction equation for both the solid and the liquid phase is:

$$(\rho C_p)\frac{\partial T}{\partial t} = \frac{\partial}{\partial x}\left(k\frac{\partial T}{\partial x}\right) + Q_a. \tag{1}$$

The volumetric source term Q_a decays exponentially from the surface, and is expressed as:

$$Q_a(x,t) = -\frac{\mathrm{d}I(x,t)}{\mathrm{d}x} = (1-R_f)\alpha\tau I_0(t)\,\mathrm{e}^{-\alpha x} \tag{2}$$

where $I(x)$ is the local radiation intensity and α is the absorption coefficient given by $\alpha = 4\pi k_{Ni}/\lambda_{exc}$. The complex index of refraction at the excimer laser wavelength is $\hat{n}_{Ni} = n_{Ni} + ik_{Ni} = 1.4 + i2.1$ [9]. For nickel at the excimer laser wavelength, the absorption depth, $1/\alpha$ is 9.4 nm. The temperature dependence of the complex refractive index of nickel is unknown to the authors, and is neglected in the calculation. The complex index of refractive of liquid nickel is unknown either; the absorption coefficient of solid nickel is used for liquid. R_t is the reflectivity at the nickel surface that is measured to be 0.28 [7]. It is noticed that the reflectivity calculated from the complex refractive index is 0.45, larger than the measured value. This discrepancy is attributed to the surface effect (oxidation, roughness, phase change, etc.).

In equation (2), $I_0(t)$ is the temporal variation of the intensity of the laser pulse, which is measured experimentally. τ is the experimentally determined transient transmissivity of the excimer laser beam through the laser-induced plume. A triangular laser intensity profile is used in the numerical computation, with the intensity increasing linearly from zero at the beginning of the pulse

to the maximum at 6 nsec, then decreasing linearly to zero at the end of the laser pulse.

Initially, the nickel target is at the ambient temperature. The boundary conduction at the top surface is treated as adiabatic. From the computation results, it is found that before the peak temperature is reached, the radiation loss at the surface is at least two orders of magnitude smaller than the incident laser intensity and the conduction heat transfer flux. After the laser pulse, the radiation flux could be on the same order of the conduction flux. Therefore, neglecting the radiation loss would over-predict the temperature after the laser pulse and the melting duration. However, the focus of this study is to obtain the peak temperature at different laser fluences. Neglecting radiation and convection would not affect the peak temperature calculation and the conclusions of this work.

3.2. Interfacial kinetic relations

As the consequence of the one-dimensional heat conduction formulation, the solid/liquid and liquid/vapor interfaces are assumed to be planar. In addition to the heat conduction equation described above, interface conditions are needed to calculate interface temperatures and interface velocities since at high laser fluences as those considered in this study, the interfaces propagate rapidly. Thus, according to the kinetic theory of phase change, the temperatures at the melting and evaporation interfaces are expected to deviate from the equilibrium melting and boiling temperatures.

At the solid/liquid interface, the relation between the interfacial superheating/undercooling temperature, $\Delta T = T_{sl} - T_m$, and the interface velocity V_{sl} is given by the kinetic theory [10]:

$$V_{sl}(T_{sl}) = C_0 \exp\left[-\frac{Q}{k_B T_{sl}}\right]\left\{1-\exp\left[\frac{-L_{sl}\Delta T}{k_B T_{sl} T_m}\right]\right\}. \quad (3)$$

When ΔT is small, equation (3) can be approximated by a linear relationship between the interface velocity V_{sl} and the superheating temperature ΔT:

$$\Delta T = C_1 V_{sl} \quad (4)$$

where C_1 is a material constant. For pure nickel, C_1 is estimated to be 1.18 K (m s^{-1}) [11]. The same superheating/undercooling model, equation (4), and the same material constant C_1 are used for melting and solidification. Differences between melting and solidification kinetics can result in different superheating–velocity relations for melting and solidification, however, this difference is neglected in this work. It will be shown by the computation results that the effect of interface superheating/undercooling has negligible effect on overall energy transfer, the temperature history, and the materials removal.

The energy balance equation at the solid/liquid interface is:

$$k_s \left.\frac{\partial T}{\partial x}\right|_s - k_l \left.\frac{\partial T}{\partial x}\right|_l = \rho_s V_{sl} L_{sl}. \quad (5)$$

At the liquid/vapor interface, assuming the two phases are in mechanical and thermal equilibrium, the specific volume of vapor is much larger than that of liquid, and the ideal gas law applies, then the Clausius–Clapeyron equation can be used to calculate the saturation pressure at the surface temperature:

$$\frac{dp}{p} = \frac{L_{lv}(T_{lv})}{R}\frac{dT_{lv}}{T_{lv}^2}. \quad (6)$$

During laser heating, the temperature of the melt can be raised thousands of degrees higher than the normal boiling point, therefore, variations of latent heat with temperature can be large. The temperature dependent latent heat is expressed as [12]:

$$L_{lv}(T_{lv}) = L_0\left[1-\left(\frac{T_{lv}}{T_c}\right)^2\right]^{1/2} \quad (7)$$

where L_0 is latent heat of evaporation at absolute zero. Equations (6) and (7) yield the following relation between surface temperature and the saturation pressure:

$$p = p_0 \exp\left\{-\frac{L_0}{R}\left[\frac{1}{T_{lv}}\sqrt{1-\left(\frac{T_{lv}}{T_c}\right)^2} - \frac{1}{T_b}\sqrt{1-\left(\frac{T_b}{T_c}\right)^2}\right] - \frac{L_0}{RT_c}\left[\sin^{-1}\left(\frac{T_{lv}}{T_c}\right) - \sin^{-1}\left(\frac{T_b}{T_c}\right)\right]\right\} \quad (8)$$

where p_0 is the ambient pressure. Note that the pressure computed from equation (8) is the saturation pressure, not the surface pressure, since the saturation pressure could be higher than the surface pressure during rapid heating (Fig. 1). The molar evaporation flux j_v at the molten surface is related to the saturation pressure as [3, 4, 13]:

$$j_v = \frac{Ap}{\sqrt{2\pi MRT_{lv}}} \quad (9)$$

where A is a coefficient accounting for the back flow of the evaporated vapor to the surface, which was calculated to be 0.82 [4, 14], i.e., 18% of the evaporated vapor returns to the surface. This return rate was computed by considering conservation of mass, momentum, and energy across a discontinuity layer (the Knudsen layer) adjacent to the evaporating surface. The liquid/vapor interfacial velocity, or the recession velocity of the target surface, V_{lv}, can be obtained from the molar evaporation flux as:

$$V_{lv} = \frac{Mj_v}{\rho_l} = \frac{AMp}{\rho_l\sqrt{2\pi MRT_{lv}}}. \quad (10)$$

The energy balance equation at the liquid/vapor interface is:

$$k_l \left.\frac{\partial T}{\partial x}\right|_l = \rho_l V_{lv} L_{lv}. \quad (11)$$

Equations (1)–(11) constitute the mathematical model describing one-dimensional laser heating, melting and evaporation.

3.3. Numerical approach

The difficulty associated with computing the phase change problem is that locations of the solid/liquid and liquid/vapor interfaces are not known as a priori. In the numerical models in literature, [e.g. 15, 16], the solid/liquid interface was directly computed; the location of the evaporating surface was obtained by a time integration of the mass flux of evaporation. Therefore, the effect of materials removal was only accounted as a surface thermal boundary condition; the effect of melt thickness reduction due to evaporation was not considered in the calculation. In the present work, a numerical model based on the enthalpy formulation is developed to track both the solid/liquid and liquid/vapor interfaces. In the enthalpy method [17], fixed grids are applied to the physical domain. Equation (1) is cast in terms of enthalpy per unit volume as:

$$\frac{\partial H}{\partial t} = \frac{\partial}{\partial x}\left(k\frac{\partial T}{\partial x}\right) + Q_a(x,t). \quad (12)$$

The interface energy balance equations are embedded in the enthalpy formulation, therefore, the interface positions are tracked implicitly. If an averaged enthalpy value H within a control volume is calculated, then it can be split into sensible enthalpy and latent heat as:

$$H = \int_{T_0}^{T} \rho c_p \, dT + f_l \rho_l L_{sl} + f_v \rho_l L_{lv} \quad (13)$$

where f_l and f_v are volume fractions of the liquid and vapor phase, respectively. In an actual situation, vapor propagates away from the surface and plays no role in the conduction process. One way to treat evaporation in fixed grids is to model the evaporation process in the same way as modeling melting, assuming that the vapor simply has the surface temperature and material properties of liquid at the surface temperature [18]. The stored energy in the evaporated zone contributes to the stability of the numerical calculation.

It is straightforward to calculate the temperature in the solid phase before melting occurs. After melting is initiated, iterations are needed to find out the interface temperatures and velocities at each time step. The procedure of the numerical calculation is described as follows:

(1) The initial temperature field is set to the ambient temperature, and the two interfacial temperatures are set to the equilibrium melting and boiling temperature T_m and T_b, respectively. Time steps are forwarded until melting occurs.
(2) When the temperature reaches the melting point, an interfacial temperature T_{sl} is assumed. For melting, the assumed interface temperature is higher than that at equilibrium. For solidification, the interface temperature is lower than that at equilibrium.
(3) Using the assumed interface temperature, the fraction of liquid phase, f_l, in each cell is calculated using iterations until the temperature field converges according to the criterion, $\max|(H_i^{new} - H_i^{old})/H_i^{old}| \leqslant 10^{-10}$. The solid/liquid interface location is then calculated from the liquid fraction number.
(4) The velocity of the solid/liquid interface is computed from the interface position obtained from Step (3). This interfacial velocity is then used to compute a new interface temperature using equation (4). If the new interface temperature differs from the value assumed in Step (2), iterations are carried out until the interface temperatures calculated from two successive iterations satisfy the convergence criterion, $|T_{si}^{new} - T_{sl}^{old}| < 10^{-4}$.
(5) When the surface temperature reaches the normal boiling point, the velocity and the temperature of the liquid/vapor interface are calculated using the same procedure as for the solid/liquid interface, indicated from Steps (2)–(4). Iterations are carried out to determine the liquid/vapor interface temperature and the evaporation rate, using the kinetic relation at the evaporating surface, equation (10), and the same convergence criteria as those used in Steps (3) and (4). When f_v is greater than 1, the cell becomes vapor. In this case, its temperature is set to T_{lv} so that the vapor does not participate in the conduction process.
(6) Steps (2)–(5) are repeated for each time step, until the solid/liquid interface velocity becomes negative (the beginning of the solidification).

In the calculation, 601 grids are fixed in a 10 μm-thick computational domain. Since the radiation absorption depth of nickel is about 10 nm and the grid size near the surface should be smaller than the absorption depth, variable grid sizes are used, with denser grids near the surface. The size of the first grid is 0.68 nm. The time increment is $\Delta t = 1 \times 10^{-11}$ s. The grid-independent test is carried out by doubling the number of grids, and no different results are found. Whenever possible, temperature dependent thermal properties are used in the calculation, which are listed in Table 1.

3.4. Numerical results and discussion

Numerical calculations are performed with the same laser parameters used in experimental studies. Results of the transient temperature field, the surface pressure, and

Table 1
Thermophysical properties of nickel used in the numerical simulation [3, 9, 13, 21, 22]

Solid density ρ_s	8900 kg m^{-3}	Liquid density ρ_l	8900 kg m^{-3}
Melting temperature T_m	1726 K	Boiling temperature T_b	3188 K
Critical temperature T_c	7810 K	Molar weight M	58.7 kg kmol^{-1}
$0.8T_c$	6248 K	Refractive index $\hat{n}_{Ni}$	$1.4+i2.1$
$0.9T_c$	7029 K	Reflection coefficient R_f	0.28
Enthalpy of fusion L_{sl}	17.6 kJ mol^{-1}	Enthalpy of evaporation L_{lv} at T_b	378.8 kJ mol^{-1}
Thermal conductivity of solid phase (W m^{-1} K^{-1})	$k_s = 114.43-0.082T$, 298 K $< T <$ 600 K; $k_s = 50.47+0.021T$, 600 K $< T <$ 1726 K		
Specific heat of solid phase (J kg^{-1} K^{-1})	$c_{ps} = -295.95+4.95T-0.0096T^2+9.46\times10^{-6}T^3-4.36\times10^{-9}T^4+7.60\times10^{-13}T^5$, 298 K $< T <$ 1400 K; $c_{ps} = 616.56$, 1400 K $< T$		
Thermal conductivity of liquid phase, k_l	89.0 W^{-1} K^{-1}	Specific heat of liquid phase, c_{pl}	734.16 J kg^{-1} K^{1}

the locations of the solid/liquid and liquid/vapor interfaces are presented as follows.

3.4.1. Transient temperature field induced by laser irradiation

Figure 5 shows transient surface temperatures at laser fluences of 2.5, 4.2, 5.2 and 5.9 J cm^{-2}. The surface temperature increases with the laser fluence, and rises quickly to the melting and boiling temperatures. Melting begins at 4.4, 3.1, 2.7 and 2.5 nsec while evaporation begins at 9.6, 5.6, 4.8 and 4.5 nsec, respectively for the four fluences. For all the four cases, the surface temperature reaches the maximum value at about 17 nsec, then decreases gradually. The peak temperatures achieved are 4022, 5974, 6553 and 7004 K. The peak temperatures at 2.5 and 4.2 J cm^{-2} are below $0.8T_c$ and the peak temperature at 5.2 J cm^{-2} is higher than $0.8T_c$ (about $0.84T_c$). At a laser fluence of 5.9 J cm^{-2}, the maximum surface temperature is about $0.9T_c$. However, as shown in Fig. 1(b), physical properties change drastically between 0.8 and $0.9T_c$. The current model does not account for these changes since property data within this temperature range are not available. When the temperature reaches $0.9T_c$, evaporation occurs as explosive phase transformation, which is not described by the current numerical model. Therefore, calculations are not performed at laser fluences higher than 5.9 J cm^{-2}.

The numerical results show a close agreement with the experimentally determined fluence when transition from surface evaporation to explosive phase transformation occurs: the numerical results indicate the surface reaches $0.9T_c$ at about 5.9 J cm^{-2}, while the experimental result shows explosive vaporization occurs at about 5.2 J cm^{-2}.

Figure 6 shows the temperature profile inside the target at different time instants, at the laser fluence of 4.2 J cm^{-2}. It is seen that the thermal diffusion depth is about 3 μm over the time period of consideration, less than the computational domain of 10 μm. It is also seen that a large temperature gradient exists near the surface for the first 30 nsec. After the laser pulse, the temperature gradient decreases. The temperature decreases with depth at all time instants. The temperature at the subsurface is higher than that at the surface by hundreds to thousands

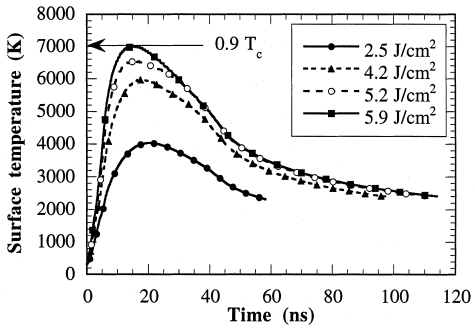

Fig. 5. Surface temperature as a function of time at different laser fluences.

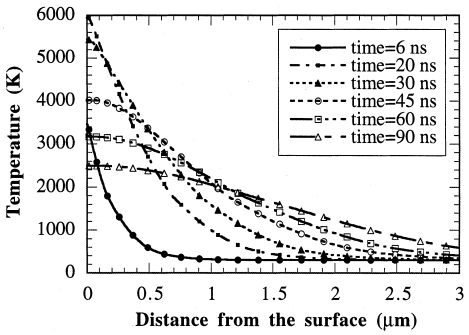

Fig. 6. Temperature profile inside the target at different time at the laser fluence of 4.2 J cm^{-2}.

of degrees, as reported by some other investigators [12, 19] is not obtained in this study.

3.4.2. Velocity of the solid/liquid and the liquid/vapor interface

Figure 7 shows variations of the melting front velocity with time at different laser fluences. The melting front velocity increases rapidly to the maximum value within a few nanoseconds. At the laser fluence of 5.9 J cm^{-2}, the maximum velocity reached is over 70 m s^{-1}. Such a high velocity is due to the high density of laser energy absorbed in the vicinity of the melt interface (near the surface) at the beginning of the melting process. As the melt interface expands into the target interior, the velocity of the melt front propagation decreases, and is dominated by heat conduction. Resolidification begins at 58, 98, 113 nsec and 115 ns, respectively at the four fluences, as the calculated melting front velocity becomes negative.

The velocity at the solid/liquid interface is limited by the interface kinetic relation [equations (3) or (4)] since a higher interface velocity corresponds to a higher melting temperature. However, the interface superheating temperature at these four laser fluences is small, less than 100 K, since the coefficient relating the superheating temperature and the interface velocity is small, 1.16 K (m s^{-1}). Numerical sensitivity studies show that the accuracy of this coefficient plays a minor role in the outcome of the calculation.

Figure 8 shows the velocity of the evaporating surface as a function of time at different laser fluences. As the surface evaporates, the velocity of the evaporating surface is dominated by the liquid/vapor interface temperature, as shown by equations (8)–(10). The maximum velocity is reached at around 17 nsec, at the same time when the maximum surface temperature is reached. Because of severe superheating of liquid near the surface at high laser fluences, there is still evaporation after laser irradiation ceases. Evaporating ends at 40, 59, 67 and 68 nsec for the laser fluences of 2.5, 4.2, 5.2 and 5.9 J cm $^{-2}$, respectively.

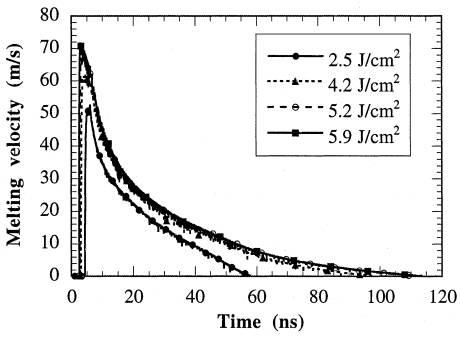

Fig. 7. Melting front velocity as a function of time at different laser fluences.

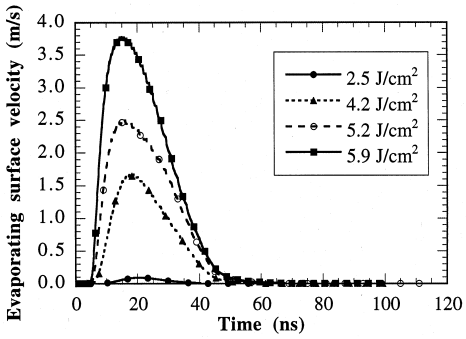

Fig. 8. Evaporating velocity as a function of time at different laser fluences.

3.4.3. Influences of uncertainties of the numerical model to the numerical results

One of the major difficulties encountered in this numerical simulation is that thermal properties at high temperatures, particularly near the critical temperature are largely unknown. Numerical sensitivity studies are carried out to determine the effect of the uncertain property data on the computational results. When the temperature is greater than $0.8T_c$, estimations of the numerical accuracy are difficult due to large variations of the reflectivity, absorptivity, density and specific heat.

In the calculation, the temperature dependence of latent heat is expressed by equation (7). This equation is in close agreement with the commonly used empirical equation given by Watson [20]:

$$L_{lv} = (L_{lv})_0 \left(\frac{1-T_r}{1-T_{r0}}\right)^{0.38} \tag{14}$$

where T_r is the reduced temperature. The two relations agree well between temperature range 3000–6000 K. For temperatures above 6000 K, the difference is below 5%. Numerical calculations show that, at the laser fluence of 4.2 J cm^{-2}, an underestimation of latent heat of evaporation by 5% increases the calculated surface temperatures by about 58 K.

The thermal conductivity data are available in the temperature ranges between room temperature and about 1500 K, as listed in Table 1. Extrapolation was used to obtain thermal conductivity between 1500 K and the melting temperature. The thermal conductivity of liquid nickel is unknown to the authors. A constant value corresponding to room temperature nickel was used in the calculation, $k_l = 89$ W m^{-1} K^{-1}, which is close to the value of solid conductivity extrapolated to the melt temperature using the equation in Table 1. Above the melting temperature, the liquid thermal conductivity was held at constant. If instead, the equation of the solid conductivity is extrapolated beyond the melting temperature to obtain the temperature dependent thermal conductivity of

liquid, then there will be about 600 K decrease in the calculated peak surface temperature for laser fluences of 4.2 and 5.2 J cm^{-2}. Therefore, the accuracy of the thermal conductivity of liquid nickel influences the numerical calculation greatly.

In the calculation, redeposition of the evaporated plume was considered by modifying the mass flux by a factor of 0.82 in equation (10). No direct measurements of the back flow of the evaporated vapor have been reported in literature. Calculations show that the back flow does not affect the peak surface temperature significantly (but it does affect the evaporation rate). The difference between the two temperature histories with and without the backflow is less than 100 K.

4. Conclusions

Pulsed laser evaporation at different laser fluence regions was studied experimentally and numerically. Time-resolved measurements were performed to determine the velocity of the laser-induced plume, and transmission and scattering of the laser beam from the plume at laser fluences between 2.5 and 10.5 J cm^{-2}. The experimental results showed that, when the laser fluence was between 5.2 and 9.0 J cm^{-2}, transmissivity of the laser beam in the laser-ablated plume and its expansion velocity changed little. Further, there was a drastic increase of scattering of laser light when the laser fluence was varied across 5.2 J cm^{-2}. All the experimental results consistently showed laser ablation was due to heterogeneous evaporation when the laser fluence was below 5.2 J cm^{-2}, and explosive phase change dominated the evaporation process when the laser fluence was higher than the 5.2 J cm^{-2} threshold value.

A numerical model for computing the transient temperature and phase change due to pulsed excimer laser irradiation was developed. This model tracked both the solid/liquid and liquid/vapor interfaces, accounting for kinetic relations at the two interfaces. The calculation agreed with the experimental results on the transition between surface evaporation and explosive phase transformation. Calculations showed that, for nickel specimens, the maximum surface temperature reached $0.84T_c$ at a laser fluence of 5.2 J cm^{-2}, and $0.9T_c$ at a laser fluence of 5.9 J cm^{-2}, while the experiments showed explosive phase transformation occurred at a laser fluence of 5.2 J cm^{-2}. The calculation also yielded the transient temperature field, the vaporization velocity and the melt front velocity. It was shown that the temperature profile inside the target decreased monotonously; the temperature at the subsurface significantly higher than that at the surface was not obtained. Influences of the uncertainties of several thermophysical properties were discussed. It was found that the interface kinetic relation at the melt interface played a minor role in this calculation. Accurate property data were needed to improve the accuracy of the numerical calculation.

Acknowledgement

Support of this work by the Purdue Research Foundation and the National Science Foundation (CTS-9624890) are gratefully acknowledged.

References

[1] A. Miotello, R. Kelly, Critical assessment of thermal models for laser sputtering at high fluences, Appl. Phys. Lett. 67 (1995) 3535–3537.
[2] M.M. Martynyuk, Phase explosion of a metastable fluid, Fizika Gorenniya i Vzryva 13 (1977) 213–229.
[3] M.M. Martynyuk, Critical constants of metals, Russ. J. Phys. Chem. 57 (1983) 494–501.
[4] V.A. Batanov, F.V. Bunkin, A.M. Prokhorov, V.B. Fedorov, Evaporation of metallic targets caused by intense optical radiation, Soviet Physics JETP 36 (1973) 311–322.
[5] W. Fucke, U. Seydel, Improved experimental determination of critical-point data for tungsten, High Temp. High Press 12 (1980) 419–432.
[6] V.P. Skripov, Metastable Liquids, John Wiley and Sons, New York, 1974.
[7] X. Xu, K.H. Song, Measurement of radiative properties of pulsed laser induced plasma, J. Heat Transfer 119 (1997) 502–508.
[8] K.H. Song, X. Xu, Mechanisms of absorption in pulsed excimer laser-induced plasma, Appl. Phys. A 65 (1997) 477–485.
[9] D.W. Lynch, W.R. Hunter, Comments on the optical constants of metals and an introduction to the data for several metals, in: E.D. Palik (Ed.), Handbook of the Optical Constants of Solids, Academic Press, Orlando, FL, 1985, p. 13.
[10] K.A. Jackson, Theory of melt growth, in: R. Ueda, J.B. Mullin (Eds.), Crystal Growth and Characterization, North-Holland, Amsterdam, 1975.
[11] G.-X. Wang, E.F. Matthys, Modeling of surface melting and resolidification for pure metals and binary alloys: effect of non-equilibrium kinetics, Proceedings of the 1995 International Mechanical Engineering Congress and Exposition, HTD-Vol. 317-2, ASME, New York, pp. 349–359.
[12] B.S. Yibas, Laser heating process and experimental validation, Int. J. Heat Mass Transfer 40 (1997) 1131–1143.
[13] M. Von Allmen, Laser-Beam Interactions with Materials, Springer Series in Materials Science, vol. 2, Springer-Verlag, Berlin, 1987, p. 204.
[14] S.I. Anisimov, Vaporization of metal absorbing laser radiation, Soviet Physics JETP 27 (1968) 182–183.
[15] J.R. Ho, C.P. Grigoropoulos, J.A.C. Humphrey, Computational study of heat transfer and gas dynamics in the pulsed laser evaporation of metals, Proceedings of the 1994 International Mechanical Engineering Congress and Exposition, Microscale Heat Transfer, HTD-Vol. 291, ASME, New York, 1994, pp. 71–90.
[16] S. Fähler, H.U. Krebs, Calculations and experiments of

material removal and kinetic energy during pulsed laser ablation of metals, Appl. Surf. Sci. 96-98 (1996) 61–65.
[17] N. Shamsundar, E.M. Sparrow, Analysis of multidimensional conduction phase change via the enthalpy model, J. Heat Transfer 97 (1975) 333–340.
[18] L.W. Hunter, J.M. Kuttler, Enthalpy method for ablation type moving boundary problems, J. Thermophysics 5 (1991) 240–242.
[19] F.P. Gagliano, U.C. Paek, Observation of laser-induced explosion of solid materials and correlation with theory, Applied Optics 13 (1974) 274–279.
[20] K.M. Watson, Thermodynamics of the liquid state, Industrial Eng. Chem. 35 (1943) 398–406.
[21] F.P. Incropera, D.P. DeWitt, Fundamentals of Heat and Mass Transfer, 3rd ed, John Wiley and Sons, New York, 1990, p. A3.
[22] I. Barin, Thermochemical Data of Pure Substances, Part II, VCH, New York, 1993, p. 1052.